Chapter 6

Overall transformation kinetics

6.1 Introduction

The model for the estimation of the growth rates of precipitates has been presented in chapter 4. Being able to predict correctly the growth rate is a first and important step; however, the overall transformation kinetics are also strongly dependent on the nucleation rate, and on the impingement effects described in chapter 3.

This chapter presents the methods used to estimate the overall transformation kinetics for multiple, simultaneous precipitation reactions in austenitic stainless steels.

6.2 Nucleation

Models for the nucleation rate have been presented in chapter 3. In the classical nucleation theory, the nucleation rate for a phase θ is given by:

$$I_\theta = N \exp\left(-\frac{G^*_\theta}{RT}\right) \nu \exp\left(-\frac{G^*_t}{RT}\right) \tag{6.1}$$

where G^*_θ is the activation energy for the nucleation of θ and G^*_t the activation energy for transfer of atoms across the $\gamma\theta$ interface; N is the number density of nucleation sites and ν is an attempt frequency taken as being kT/h. For a spherical precipitate θ, the activation energy for nucleation is given by:

$$G^*_\theta = \frac{16\pi}{3} \frac{\sigma^3_{\gamma\theta} {V^\theta_m}^2}{\Delta G^2_{m,\theta}} \tag{6.2}$$

where $V_m^{\theta\,2}$ is the molar volume of θ, $\sigma_{\gamma\theta}$ the energy per unit area of the interface γ/θ, $\Delta G_{m,\theta}$ the driving force for the precipitation of θ, per mole of components in θ. This unusual reference is prompted by the need to use a definition compatible with MT-DATA, in which the most reliable reference quantity is not the number of moles of a phase but the number of moles of components in a phase. Most of the times, these quantities are different, as for example, 1 mole of components in TiC corresponds to 0.5 mole of the phase. The molar volumes need to be defined accordingly, with, in the case of interstitial phases such as austenite, an additional complication introduced by the fact that not all component contribute to the volume, but only the substitutional one. However, calculating the number of moles of substitutional elements with MT-DATA is not a difficulty.

6.2.a Calculating the driving force for nucleation

The Gibbs energy change for precipitation reaction $\gamma \longrightarrow \gamma\prime + \theta$, where $\gamma\prime$ refers to austenite with a composition different from that of γ, can be written:

$$(n_0 - n_\theta)G_{\gamma\prime} + n_\theta G_\theta - n_0 G_\gamma \tag{6.3}$$

where n_0 is the initial number of moles of components in γ, n_θ the number of moles of components in θ at equilibrium and G_θ the Gibbs energy of θ per mole of component.

In most cases, the molar Gibbs energy of the precipitate is actually higher than that of the parent phase, and the main contribution to the driving force comes from the composition change of the latter. Table 6.1 illustrates this by giving examples of molar Gibbs energy for austenite, $M_{23}C_6$ and σ-phase. Obviously, the driving force for nucleation

	Austenite	$M_{23}C_6$	σ-phase
Gibbs energy (J/moles of components)	-50.53×10^3	-50.96×10^3	-45.99×10^3

Table 6.1: The molar Gibbs energy of austenite, $M_{23}C_6$ and σ-phase for a steel of composition 18 Cr, 12 Ni, 1 Mo, 1.5 Mn, 0.4 Si, 0.5 Nb, 0.05 Ti, 0.06 C wt%, at 750 °C. The formation of σ-phase is essentially justified by a reduction of the austenite molar Gibbs energy, rather than the formation of a phase of lower Gibbs energy as is the case for $M_{23}C_6$.

can not be estimated by $G_\theta - G_\gamma$ as this would imply that σ-phase never forms in alloys in which it is expected. The composition change contribution must be included, so that the driving force is best estimated by equation 6.3, divided by n_θ.

An additional difficulty has been presented in chapter 3: the most probable composition for the nucleus of θ is that for which the driving force for nucleation is maximum. However the method of the parallel tangents becomes increasingly difficult to implement mathematically as the number of components increases; furthermore, the Gibbs energy of the phases involved is not easily accessible as an analytical function of the composition. Approximating G_θ to the equilibrium value is however reasonable in these systems, since precipitates tend to have a very limited domain of existence, *ie* very sharply peaked Gibbs energy curves in the composition space. This is illustrated in figure 6.1. For the limit corresponding to fixed composition compounds, there is no difference.

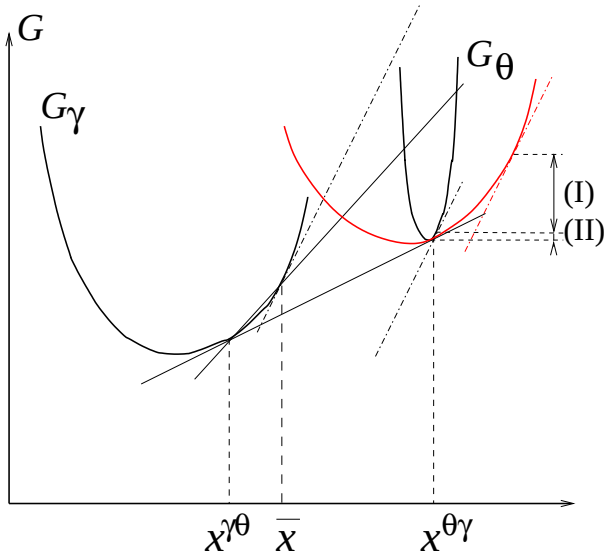

Figure 6.1: The parallel tangent construction as explained in chapter 3, for two cases: for precipitates, which often have limited domains of existence over the compositions space, approximating G_θ to the equilibrium value leads only to a small error (II). When θ is a more extended solid solution, the Gibbs energy of the most probable composition can be significantly different from that of the equilibrium composition (I).

Because the FORTRAN computer program written to model the precipitation kinetics is interfaced directly with MT-DATA, a software package to perform thermodynamic calculations with the use of the SGTE databases, it is possible to calculate the driving force for nucleation at each stage of the precipitation sequence. This avoids assumptions as to its evolution with time as needed to be made in the programs developed by Robson and Bhadeshia [88], or Fujita and Bhadeshia [93]. In these models, the initial driving force had to be given as an input, and the program then assumed a linear decrease as the

	$\Delta G_{m,\sigma}$
At $t = 0$	-77.7 J/mol
After formation of NbC and TiC	-130.0 J/mol

Table 6.2: The driving force for nucleation of σ-phase at the onset of precipitation, and after precipitation of TiC and NbC in an alloy of composition 18 Cr, 12 Ni, 1.0 Mo, 1.5 Mn, 0.5 Nb, 0.05 Ti, 0.06 C wt%, at 750 °C. The carbon depletion caused by TiC and NbC causes an increase in the driving force for σ-phase formation. Effects of this type cannot be identified when only the initial driving force is provided to the program which then assumes it to decrease with the supersaturation of Cr (in the case of σ phase).

supersaturation is reduced. By this method, it is impossible to grasp effects such as that of carbon on the formation of σ-phase: when carbon precipitates as NbC or TiC, the driving force for σ-phase formation is increased, although the supersaturation of chromium, the principal alloying element forming σ-phase, is not affected.

The use of MT-DATA as a slave application allows such interactions to be properly taken into account as a function of time, without any assumption about the evolution of the driving force or the precipitation sequence.

6.2.b The unknowns in the nucleation rate

The parameters N, $\sigma_{\gamma\theta}$ and G_t^* in equation 6.1 have to be determined for each phase in order to calculate the nucleation rate. The values that can be attributed to these parameters are bounded by physical considerations and comparisons. G_t^* can be attributed the value of the activation energy for self-diffusion of the principal element entering the precipitate, while the literature can also provide approximate values for the interfacial energy between precipitate and matrix.

However, because of the large influence these parameters have on the nucleation rate, in particular N, the most important constraints derive from the need to obtain a sensible evolution of the volume fraction of the precipitates. The parameters N and σ are therefore best seen as fitting parameters.

Figure 6.2 illustrates the influence of N, the nucleation site density, and $\sigma_{\gamma\theta}$, the interface energy per unit area, for the formation of $M_{23}C_6$ in an AISI 316 steel at 800 °C. Both have a considerable influence on the overall transformation rate, with up to 8 orders

of magnitude difference when the interfacial energy changes between 0.15 and 0.25 J/mol.

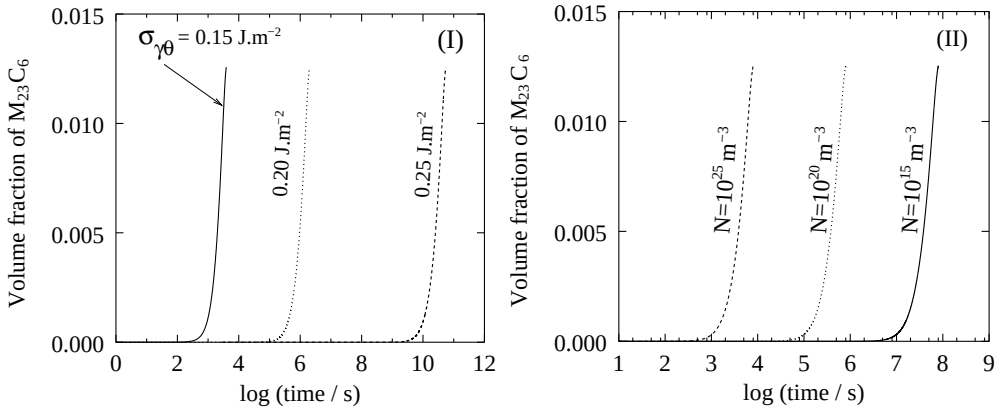

Figure 6.2: The effect of (I) the interfacial energy $\sigma_{\gamma\theta}$ with $N = 10^{19}$ m^{-3} and (II) the nucleation site density N with $\sigma_{\gamma\theta} = 0.2$ J m^{-2} on the the overall kinetics of $M_{23}C_6$ formation in an AISI 316 steel, all calculations are for 800 °C.

Although there is a considerable amount of literature regarding precipitation in austenitic stainless steels, there is virtually no reliable quantitative study of the precipitation sequence. Identical difficulties in obtaining volume fraction have been met in this work and are presented in chapter 8. The published literature mostly reports TTP (time temperature precipitation) diagrams such as figure 2.7. Such diagrams do not provide quantitative data since they neither indicate the end of precipitation, nor the exact start: there is no standard quantity defining the onset of precipitation, which depends on the experimental methods used.

The values adopted later are therefore based on an attempt to match predictions with general observations reported in TTP diagrams.

6.3 Overall transformation kinetics

To estimate the overall transformation kinetics, it is necessary to account for both soft and hard impingement. Figure 6.3 illustrates, in a simplified manner, the functioning of the FORTRAN program interfaced with MT-DATA, used to estimate the overall kinetics of simultaneous precipitation reactions.

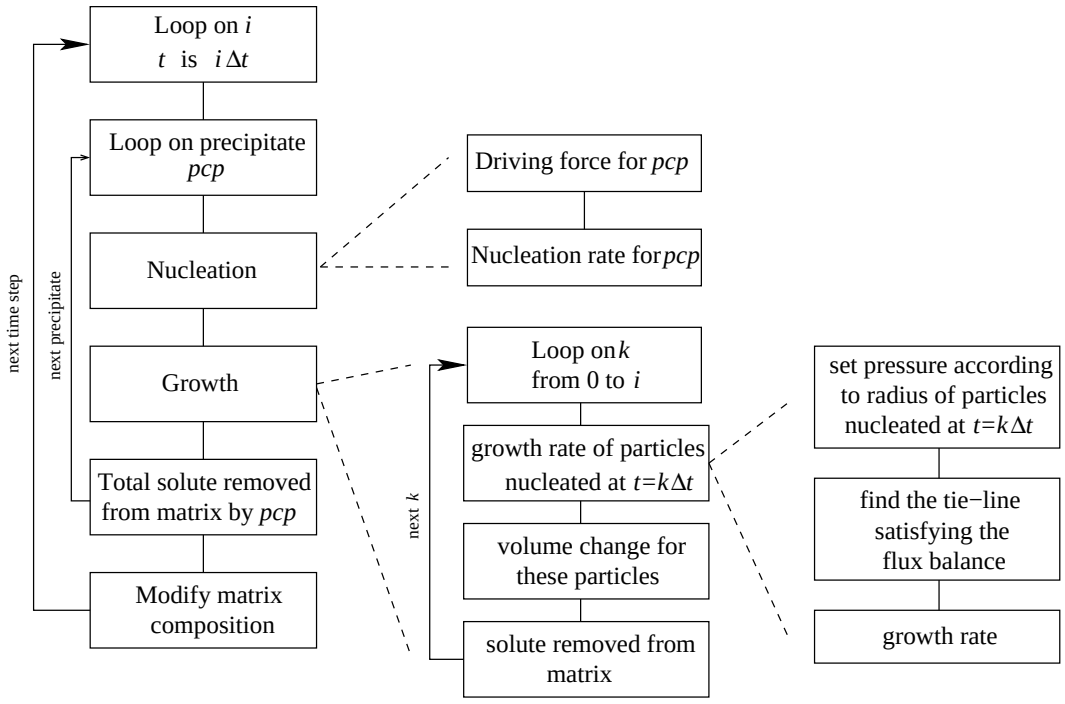

Figure 6.3: Simplified illustration of the functioning of the FORTRAN program written to estimate the evolution of simultaneous precipitation reactions. t is the time and Δt the increment, pcp is a variable identifying the phases allowed to form.

During a time step, the program considers in turns all the different phases allowed to enter the calculation, and calculates the volume increase from each of them. This increment, is, as explained in chapter 3, an extended volume, and has to be corrected according to [88]:

$$\mathrm{d}V^{f,\theta} = \left(1 - \sum_{k} V_{f,k}\right) \mathrm{d}V^{e}_{f,\theta} \tag{6.4}$$

where $\mathrm{d}V_{f,\theta}$ is the change in volume fraction of θ, $V_{f,k}$ the volume fraction of precipitate k, and $\mathrm{d}V^{e}_{f,\theta}$ the change in extended volume fraction of θ. However, in the present case, this

correction is of negligible consequence, as precipitation phenomena involve small volume fractions.

Consider component i, for which the amount $\overline{c_i}V_{f,\gamma}+\sum_k V_{f,k}c_i^{k\gamma}$ is constant due to mass conservation, and therefore, the matrix composition changes according to the increment of precipitate θ (noting that $V_{f,\gamma} = 1 - \sum_k V_{f,k}$) as follows:

$$\mathrm{d}\overline{c_i} = \frac{\left(\overline{c_i} - c_i^{\theta\gamma}\right)\mathrm{d}V_{f,\theta} - \overline{c_i}}{V_{f,\gamma}} \tag{6.5}$$

where $\mathrm{d}\overline{c_i}$ is the change of matrix composition. This quantity is calculated in turn for each precipitate, and the matrix composition is updated at the end of the time step. The program also verifies that the composition change is small compared to the content of the matrix, so as to ensure the step size is not too large.

The method described in figure 6.3 requires significant computing power. Each loop to identify a tie-line can take up to 50 iterations (figure 4.4), each including an equilibrium calculation. This is repeated as many times as is the current time step, that is, step 1000 requires 1000 iterations to calculate the growth rate of all the precipitates nucleated at earlier times. The whole process is also repeated as many times as there are precipitates. Typical calculation times are 2-3 days on 64 bits, 450 MHz processor machine. When capillarity effects are neglected, however, the tie-line is unique to all precipitates of the same nature and there is no need to calculate one for each different nucleation time.

6.4 The tie-line shifting phenomenon

As explained in chapter 4, the composition of precipitates such as $M_{23}C_6$ is expected to be modified by the need to satisfy the flux balance at the interface matrix/precipitate. The tie-line satisfying the flux-balance at the onset of precipitation does not generally go through the bulk composition. However, as the precipitation reaction progresses, the matrix composition is modified, and as a consequence, the tie-line satisfying the flux-balance shifts towards the one going through the bulk composition P (figure 6.4).

Many studies have reported composition changes in $M_{23}C_6$ as its precipitation progresses [100, 67, 104]: the Cr content increases while the Fe content decreases. This was correctly reproduced by the model, as illustrated in figure 6.5, which shows the Cr and Fe content of $M_{23}C_6$ in an AISI 316 steel, as precipitation progresses.

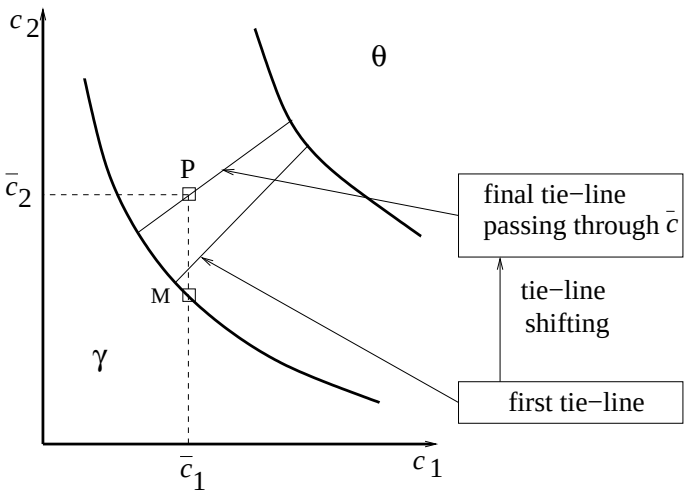

Figure 6.4: Illustration of the tie-line shifting phenomenon. As the supersaturation of elements 1 and 2 decreases, the tie-line satisfying the flux-balance approaches that going through point P, the bulk composition.

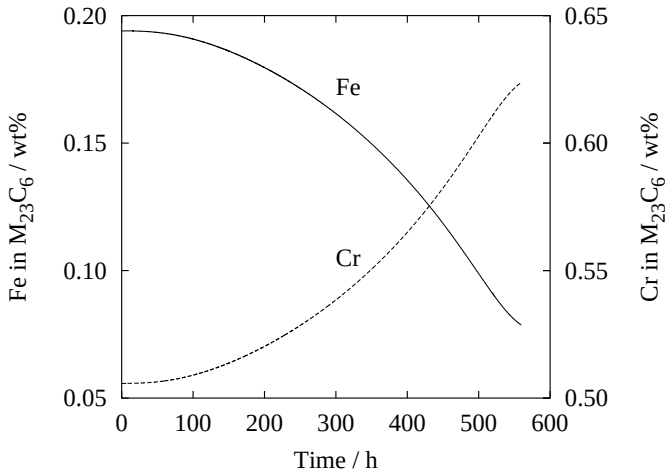

Figure 6.5: Verification of the tie-line shifting phenomenon during the precipitation of $M_{23}C_6$ in an AISI 316 steel at 800 °C. The initial Fe content is larger than expected from an equilibrium calculation, while the Cr is lower. As precipitation reaches completion, both the Fe and Cr contents return to their equilibrium values.

Similar observations have been made for MC type carbides (e.g. NbC, TiC), as mentioned in chapter 2: these carbides grow with a chromium content much larger than is the equilibrium value, and with a carbon content below a 1:1 atomic stoichiometry. However, because they are modelled as pure substances in the SGTE databases, it is not possible to reproduce these composition changes.

6.5 Multiple precipitation reactions

One of the main advantages of the model developed is its ability to cope with as many simultaneous precipitation reactions as required by the user, provided that thermodynamic data are available in the databases used by MT-DATA.

6.5.a Precipitates drawing from the same solute

The various phases likely to form in austenitic stainless steels frequently draw on one or two similar solutes. For example, $M_{23}C_6$ and TiC compete for carbon, σ-phase and $M_{23}C_6$ for chromium, *etc.*

When strong carbide formers such as Ti or Nb are added in sufficient quantities, $M_{23}C_6$ is not expected to be present at equilibrium. It is however usual to observe the latter forming at early stages of the ageing. The AISI 321 steel (17.1Cr, 12.6Ni, 1.5Mn, 0.5Si, 0.49Ti, 0.11C wt%) as studied by Thorvaldsson [105] is a good example of the importance of interactions in precipitation sequences. Table 6.3 gives the equilibrium state, as calculated with MT-DATA for this steel, at 750 °C.

Phase	volume fraction / %
σ-phase	0.058
TiC	0.74

Table 6.3: The equilibrium at 750 °C for the AISI 321 steel studied by Thorvaldsson *et al.* [105], calculated with MT-DATA.

It is noticeable the σ-phase is predicted to be present at equilibrium, although there is no driving force for its formation when considering the transformation of the initial austenite, or even after solution treatment at 1250 °C. Table 6.4 gives the austenite composition after solution treatment at 1250 °C.

Element		Cr	Ni	Mn	Si	Ti	C
Bulk composition	**wt %**	17.2	12.6	1.5	0.5	0.49	0.11
After sol. treat.	**wt %**	17.14	12.63	1.503	0.501	0.302	0.063

Table 6.4: The bulk composition and the austenite composition after solution treatment at 1250 °C for the AISI 321 steel studied by Thorvaldsson [105].

As illustrated in figure 6.6, the kinetics of formation of TiC are affected by the formation of $M_{23}C_6$, which also draws carbon from the matrix. $M_{23}C_6$ is not expected as an equilibrium phase, but forms for kinetic reasons.

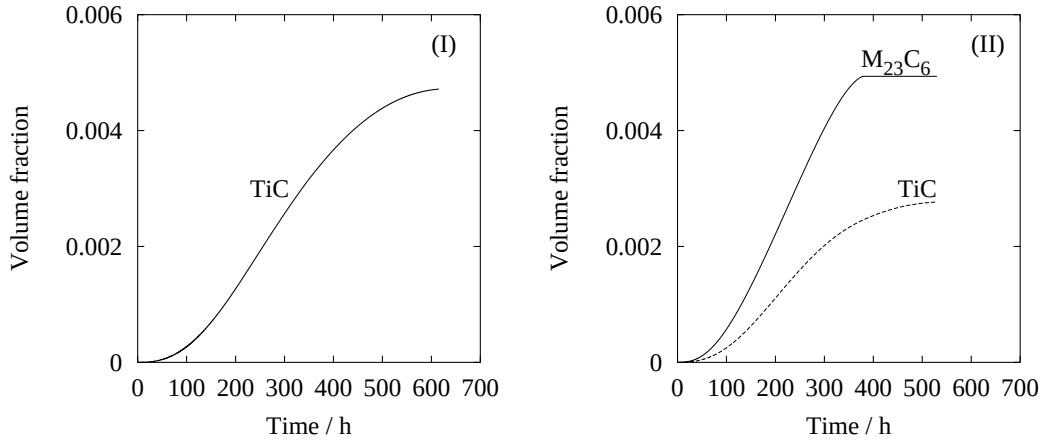

Figure 6.6: The predicted kinetics of formation of TiC in the AISI 321 steel studied by Thorvaldsson [105], (I) allowing only TiC and (II) allowing $M_{23}C_6$ and TiC, showing clearly the interactions as the two precipitates compete for carbon. $M_{23}C_6$ is not expected to be an equilibrium phase but forms for kinetics reasons.

Although interactions between precipitates are expected such as those presented in figure 6.6, a valid prediction is still required to show TiC as the only phase remaining after sufficient ageing, as given by the equilibrium calculation. For this, the model needs to account for the dissolution of transient phases.

6.5.b Dissolution of precipitates and transient phases

To illustrate the method used to implement the dissolution of precipitates, the example of the AISI 321 steel above is used again.

Figure 6.6 (II) shows that, after some time, $M_{23}C_6$ precipitation reaches completion. However, TiC, more stable than $M_{23}C_6$ according to MT-DATA, keeps on drawing carbon from the matrix, leading to the situation illustrated in figure 6.7: when precipitation of $M_{23}C_6$ is completed, the composition of the matrix is given by M′, which is on the tie-line going through the bulk composition P. This tie-line shifting phenomenon was explained previously. During the next time step, TiC draws carbon from the matrix, explaining the shift (1) of point M′, but also increases its own volume fraction. Since the matrix chromium content is not affected by the formation of TiC, but its volume fraction is

slightly reduced, the chromium concentration, and of any other element not included in TiC, is increased. This explains the shift (2) in the change from M′ to M″.

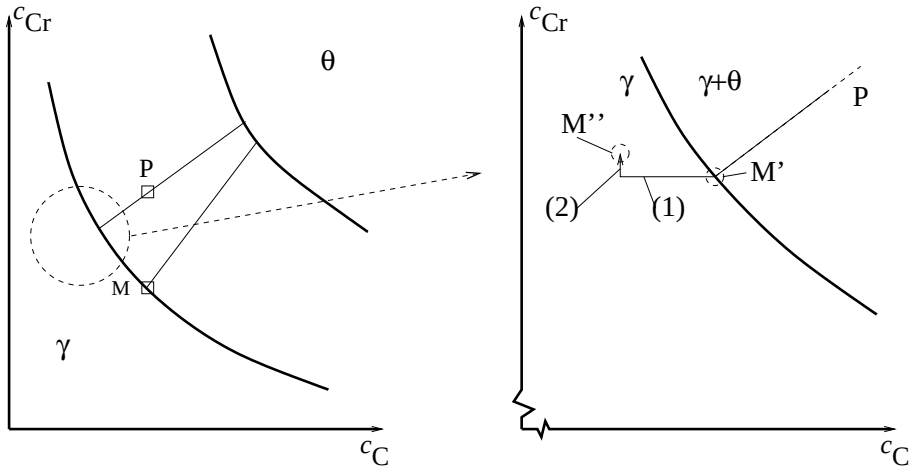

Figure 6.7: Illustration of the matrix composition change resulting from the continued formation of TiC when $M_{23}C_6$ precipitation is completed.

It is important to notice that both shifts (1) and (2) are very small, as they correspond to the quantity of solute drawn during a single time step, the latter being set so as to prevent composition modifications which are not negligible compared to the matrix content, as explained earlier. Here again, the tie-line giving the interface composition during dissolution is expected to be the one respecting the iso-activity of carbon. However, because M″ is very close to M′, the shift is of negligible proportion. Another consequence is that the supersaturation (although negative) is very small, and therefore simplified model such as Zener's approximation presented in equation 3.26 can be used.

The case when a phase dissolves with a larger negative supersaturation is different and cannot be treated with these approximations. For example, when $M_{23}C_6$ formed during service at about 700 °C is dissolved during solution treatment at 1200 °C, the point representing the bulk composition in the phase diagram is at a non-negligible distance from the $\gamma/\gamma + \theta$ boundary. Therefore the above treatment for the dissolution of phases is essentially valid for transient phases.

Figure 6.8 illustrates the predicted behaviour of the AISI 321 steel whose composition is given in table 6.4. Comparisons with experimental results are reasonably satisfying, since results by Thorvaldsson *et al.* [105] suggest that, for this steel, precipitation of TiC is completed after about 1000 h. However, the authors report a dissolution of TiC for

$M_{23}C_6$ and not the opposite. As reported in chapter 2, this observation is controversial. The dissolution cannot be predicted if the phase stability calculations indicate TiC as the equilibrium precipitate.

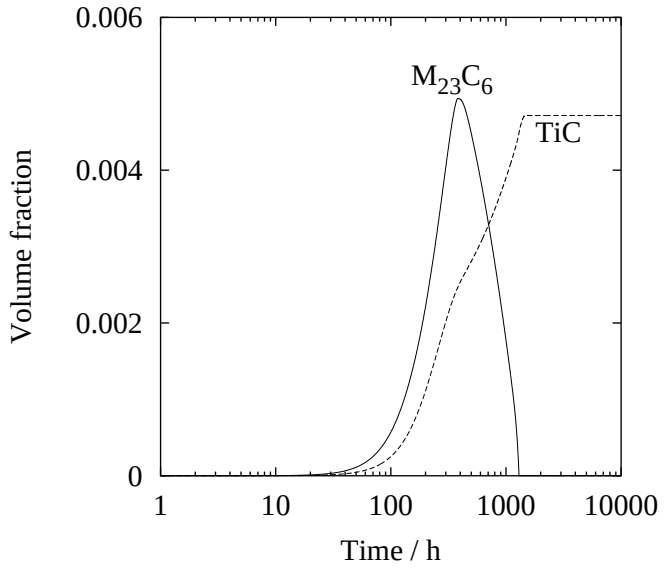

Figure 6.8: The calculated volume fraction of $M_{23}C_6$ and TiC as a function of time in an AISI 321 steel, during ageing at 750 °C. $M_{23}C_6$ is expected as a transient phase only. The volume fraction of TiC does not include the amount left undissolved after solution treatment.

Table 6.3 shows that σ-phase is also expected at equilibrium in the considered AISI 321 steel. However, it is neither predicted by the present model nor observed by Thorvaldsson [105]. The model does predict a non-zero driving force for its formation, when precipitation of TiC has almost reached completion. This is because both the low carbon and high chromium expected at that stage are favourable to σ-phase formation. Nevertheless, this driving force is too low for the formation of σ-phase to occur in an observable time.

6.6 Predicting the behaviour of different steels.

As mentioned earlier, there is little quantitative information regarding precipitation in austenitic stainless steels. Furthermore, results obtained by different methods differ significantly. For example, the work used in the previous section, from Thorvaldsson and

Dunlop [105], indicates that the maximum volume fraction of MC type carbides is reached after about 1000 h, on the basis of TEM investigations. On the other hand, Thorvaldsson *et al.* [104], in a different publication on a similar steel, in identical conditions, report the maximum volume fraction of MC type carbides to be reached after 3 to 8 hours, on the basis of resistance measurement.

This renders difficult if not impossible the task to estimate the adjustable parameters N and $\sigma_{\gamma\theta}$ for these phases. However, the time scale for the formation of such carbides and nitrides remains small in comparison with the typical lifetime, and therefore the error introduced in the precipitation sequence is of little consequence.

6.6.a The formation of σ-phase in the AISI 300 series

The case of σ-phase, which incidentally is believed to be more relevant to long term creep properties than the various carbides, is better defined. Minami *et al.* [44] provide data on the microstructural evolution of the main AISI 300 series steels, which have been used to refine the parameters N_σ and $\sigma_{\gamma\sigma}$. The use of equation 6.1 to predict the nucleation rate for σ-phase leads however to meaningless values of these parameters: only with interfacial energies close to zero and extremely large N_σ would a sufficient nucleation rate be obtained. Observation of σ-phase in such steels also indicates a difficulty in nucleation, as this phase is almost exclusively found on grain boundary triple points.

A simple model was therefore used to estimate triple point nucleation. Triple point nucleation can be integrated within the model without loss of consistency: the points can be assumed to be uniformly distributed in space and therefore the treatment of the hard and soft impingement remains valid. This is not the case for grain surface nucleation, where both soft and hard impingement effects may be strongly localised.

A simple modification to equation 3.20 was done to account for the extra amount of grain boundary surface eliminated when nucleation occurs on a triple point:

$$G_B^* = \frac{4}{27}\frac{\left\{\eta_{\gamma\theta}\,\sigma_{\gamma\theta} - \frac{3}{2}\eta_{\gamma\gamma}\,\sigma_{\gamma\gamma}\right\}^3}{\eta_\theta{}^2 \Delta G_v{}^2} \tag{6.6}$$

where the different terms are as defined in equations 3.21.

6.6.b σ-phase in AISI 304

The case of AISI 304 is interesting to start with because σ-phase is the only phase expected, with the exception of $M_{23}C_6$ which is precipitated in the very early stages of

ageing. The absence of interaction with other precipitation phenomena simplifies greatly the determination of the parameters N_σ and $\sigma_{\gamma\sigma}$.

i Parameters optimisation

For a given ageing temperature, there is an infinite number of combinations of parameters $N_\sigma, \sigma_{\gamma\sigma}$ to obtain a similar result for the volume fraction as a function of time. For example, a greater interfacial energy renders nucleation more difficult but N_σ can be raised to compensate.

However, if N_σ and $\sigma_{\gamma\sigma}$ have been chosen too large for example, the nucleation rate will be overestimated at lower temperatures and, and underestimated at higher temperatures. Therefore, values for N_σ and $\sigma_{\gamma\sigma}$ have to be obtained that fit published data over a range of temperatures.

For N_σ, a first guess can be made by estimating the number of triple points per unit volume ($10^{10} - 10^{14}$ m^{-3}), while the value of the interfacial energy for a grain boundary was used as a starting point for $\sigma_{\gamma\sigma}$.

ii Results

With $N_\sigma = 3 \times 10^{12}$ m^{-3} and $\sigma_{\gamma\sigma} = 0.283$ J/m^2, good agreement could be obtained between the predictions and both the time temperature precipitation diagram and the quantitative measurements obtained by Minami *et al.* [44], as illustrated in figure 6.9.

The disagreement at high temperatures is essentially due to thermodynamic data on which the model rely: MT-DATA predicts an equilibrium amount of σ-phase which is not consistent with the observation made by Minami *et al.*, and it is therefore not surprising that the kinetics of its formation is underestimated.

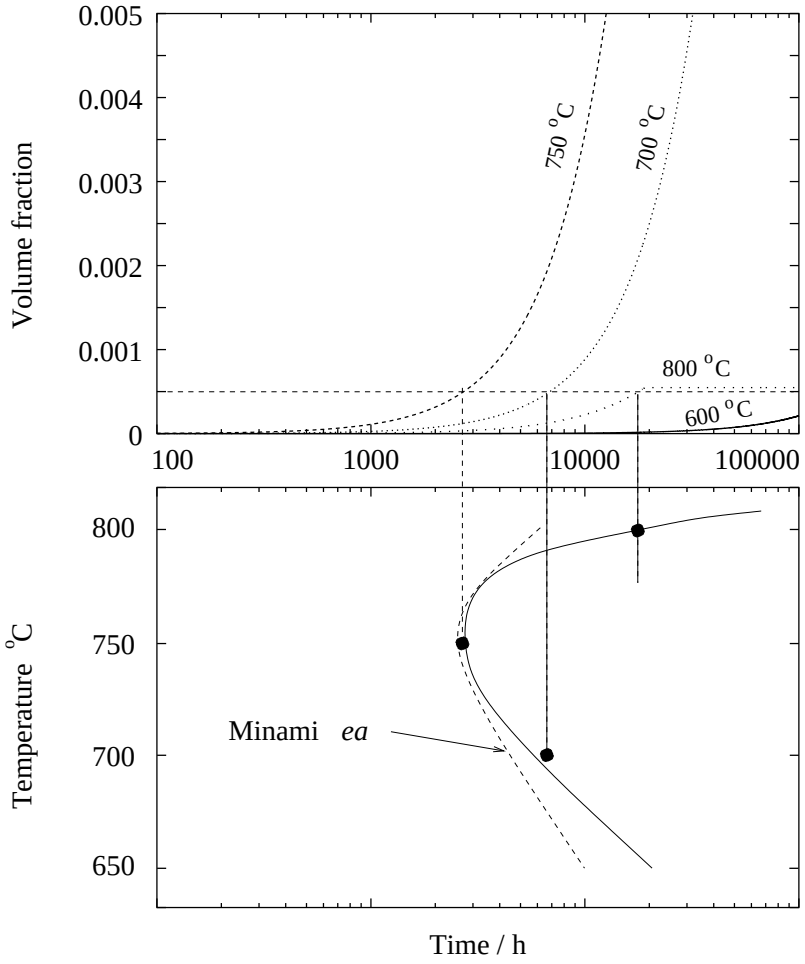

Figure 6.9: TTP (Time Temperature Precipitation) diagram for the formation of σ in an AISI 304 steel of composition: 18.7Cr, 9.0Ni, 1.73Mn, 0.6Si, 0.05C wt%. Predictions are compared to the TTP diagram obtained by Minami *et al.* [44]. The detection limit is assumed to be a volume fraction of 0.05 %. $M_{23}C_6$ is found at all times and temperatures, both experimentally and in predictions.

6.6.c Other steels in the AISI 300 series

i Observed and predicted trends

Figure 6.10, after [44] shows the evolution of the volume fraction of σ-phase as a function of ageing time at 700 °C, in different steels of the AISI 300 series. It has been proposed that the very low carbon level of the austenite in steels such as AISI 321 or AISI 347 is responsible for the rapid formation of σ-phase (chapter 2).

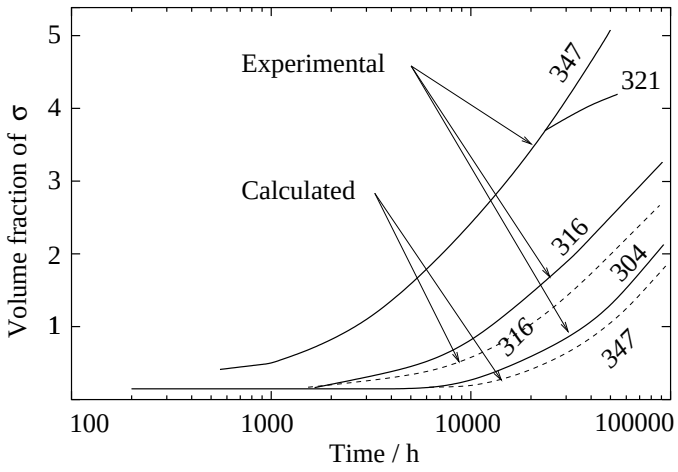

Figure 6.10: The rate of formation of σ-phase at 700 °C in different steels of the AISI 300 series, after [44]. Both 321 and 347 contain strong carbides formers (Ti and Nb respectively) which reduce the austenite carbon content to almost zero. Dashed lines show the predictions with the parameters obtained by fitting the curve for the AISI 304 steel.

Because of variations in the grain size, or thermo-mechanical history, it is probable that the values of N_σ and $\sigma_{\gamma\sigma}$ will have to be slightly adjusted. However, with the exception of AISI 316 in which σ-phase is predicted to form slightly faster than in AISI 304, the predictions show a trend opposite of that reported by Minami *et al.* [44], as illustrated in figure 6.10: σ-phase is predicted to form at a slower rate in AISI 321 and 347. Table 6.5 shows the driving force for the formation of σ-phase in these different steels, at the end of the carbides formation, where it is expected to be greatest.

The prediction of a slower formation of σ-phase in AISI 321 and 347 compared to 304 can therefore be expected from the thermodynamic data underlying the model, since the classical theory for nucleation predicts a greater nucleation rate when the driving force is larger.

It seems reasonable to assume that the growth rate of σ-phase does not vary signifi-

Element wt%	Cr	Ni	Mn	Si	Ti	Nb	C	ΔG_m J/mol
AISI 304	18.20	9.07	1.73	0.60			2.15×10^{-3}	-209.7
AISI 347	17.68	10.45	1.65	0.59		0.48	4×10^{-5}	-169.7
AISI 321	17.64	10.53	1.76	0.59	0.15		6×10^{-5}	-176.1
AISI 316 (2.3 Mo)	16.09	12.01	1.83	0.64			5.4×10^{-4}	-288.4

Table 6.5: The composition of 4 different steels studied by Minami *et al.*, after precipitation of all carbides, calculated with MT-DATA, and the driving force for the formation of σ-phase from the austenite of this composition, expressed in joules per mole of components. All calculations are for 700 °C.

cantly between the different steels; this is supported by the fact that the slopes in figure 6.10 are similar. Therefore, as already proposed in the literature (e.g. [67]), the cause is most likely to be found in the nucleation process, although the above results on the driving force indicate that classical theory may not provide an explanation.

ii Is the classical theory for nucleation failing ?

The former section indicates that, although the driving force for the nucleation of σ-phase is expected to be lower in AISI 347 when compared to AISI 304, nucleation actually occurs significantly faster in the former.

Because the different steels present reasonably similar nucleation site densities, it seems justified to propose as above, that the prefactor N in the nucleation rate equation 6.1 does not vary significantly between two steels. However, further examination of the classical theory will reveal that this assumption may be erroneous.

One of the first steps of the nucleation theory consists in counting the number of nuclei which have reached the critical radius, and to which is associated an energy G^*_θ, as explained in chapter 3. This is done by assuming that the probability of finding such nuclei is given by a Boltzmann distribution:

$$N_{critical\ nuclei} \propto \exp\left(\frac{-G^*_\theta}{RT}\right) \tag{6.7}$$

However, it must not be forgotten that such an equation actually gives the probability for a fluctuation of composition/structure of energy G^*_θ. For the sake of simplicity, structure fluctuations are neglected in the following discussion.

In a binary alloy, there is an equivalence relationship between a composition fluctuation of given spatial extension, and a fluctuation of given energy. This is illustrated schematically in figure 6.11.

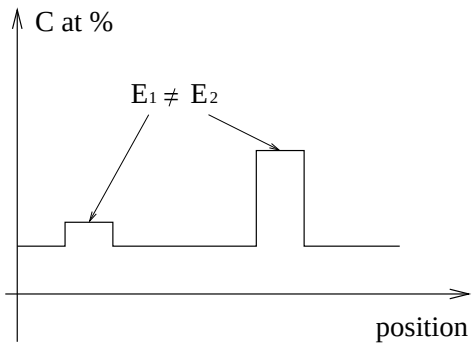

Figure 6.11: In a binary alloy, for example Fe-C, fluctuations of the carbon content are uniquely associated to an energy which can therefore be written E(C).

In this case, it is reasonable to assume that the prefactor N does not include any composition dependencies, which are all present in the exponential term.

The situation is however different in multicomponent alloys. In the following, the hypothetical case of the nucleation of σ-phase in a Fe-Cr-C system is considered as an example and fluctuations in both the carbon and chromium content are examined. As illustrated schematically in figure 6.12, a number of different fluctuations may have the same energy.

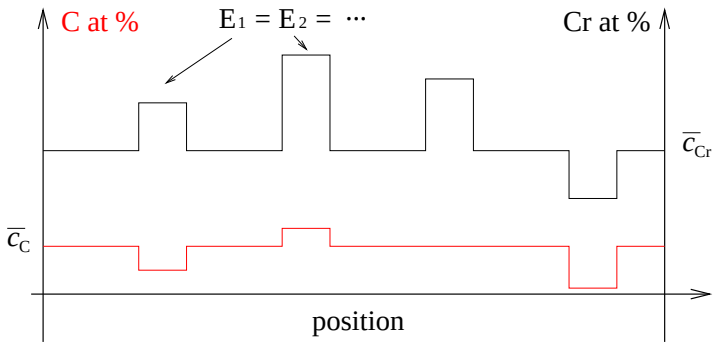

Figure 6.12: Schematic illustration of composition fluctuations in a Fe-Cr-C alloy. Different fluctuations may be associated with the same energy, but not all are events leading to the formation of a nucleus.

However, only a fraction of the composition fluctuations of energy G^*_θ is of interest for the nucleation of σ-phase. Therefore, the probability to form a critical nucleus is better written $f \exp(-G^*_\theta/RT)$ than $\exp(-G^*_\theta/RT)$, where f is the fraction of the fluctuations of

energy G_θ^* that may lead to the formation of σ-phase. Equation 6.1 can then be re-written:

$$I_\theta = f N_0 \exp\left(-\frac{G_\theta^*}{RT}\right) \nu \exp\left(-\frac{G_t^*}{RT}\right) \tag{6.8}$$

This never appears in practice since the prefactor is fitted as a single entity, and it is probably difficult to estimate f on a theoretical basis.

It is now considered, as a simple model, that composition fluctuations leading to the formation of a σ-phase nucleus are those raising simultaneously the Cr content above, and lowering the C level below, critical values, since the carbon solubility in σ-phase is close to zero. Figure 6.13 illustrates two different cases: when the average carbon content of the austenite ($\overline{c_C}$) is relatively high, the fraction of the fluctuations of identical energies which brings the carbon content below the critical level is smaller than when $\overline{c_C}$ is low.

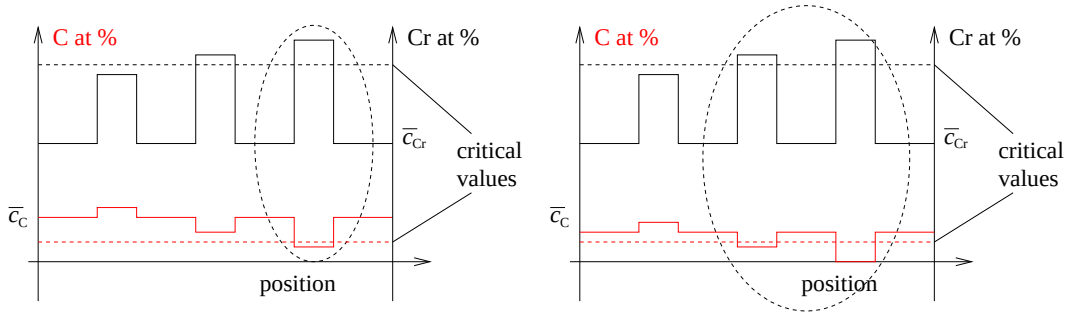

Figure 6.13: Schematic illustration of different composition fluctuations in two cases. The fractions of the fluctuations which can lead to the nucleation of σ-phase is higher when the average carbon content of the austenite is lower.

Using again the calculated carbon content of the austenite (table 6.5), and attributing a factor f_{304} and f_{347} to the steels of same names, we can expect, on the basis of the above argument, $f_{304} \ll f_{347}$ since the austenite carbon content is much lower in the AISI 347 steel. Having fitted $N_{\sigma,304} = N_0 f_{304}$ to experimental data, it is now expected that the prefactor $N_{\sigma,347} = N_{\sigma,304}(f_{347}/f_{304})$ be much larger than $N_{\sigma,304}$.

Further validation is obtained when considering the case of the AISI 316 steel, in which the rate of σ-phase formation is also under-estimated. Following identical reasoning, and since the austenite carbon content is lower in the AISI 316 steel than it is in 304 (table 6.5), the fraction f_{316} is expected to be larger than f_{304} and consequently the prefactor $N_{316} = N_{304}(f_{316}/f_{304})$ larger than the experimentally derived N_{304}. This would lead to a shift to the left of the curve, consistent with observations.

Finally, the tendency to underestimate the kinetics of σ-phase formation at lower temperatures for the reference steel, as visible in the TTP diagram 6.10, could also be explained by the austenite carbon content decreasing with the temperature, as shown in figure 6.14.

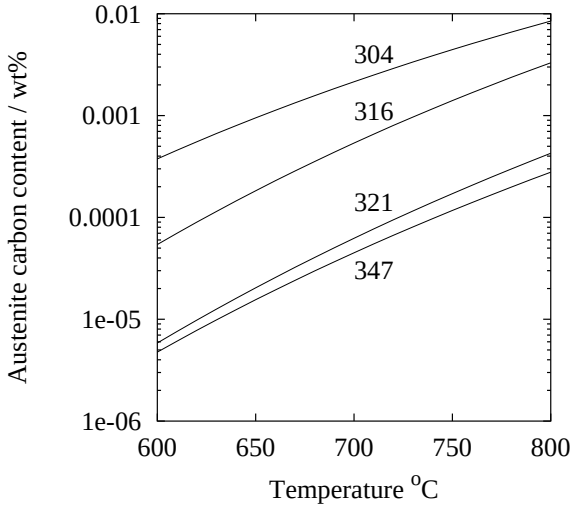

Figure 6.14: The carbon content of the austenite after precipitation of all carbides in different steels from the AISI 300 series, calculated with MT-DATA.

Figure 6.15 shows that better agreement is obtained for increasing N as the carbon content decreases. However, due to the restricted amount of quantitative data available, it was not possible to obtain a relationship between N and the carbon content of the austenite. Such a relationship would only hold for a given steel, as the introduction of additional elements such as Mo should, according to the explanation proposed above, further modify the prefactor N.

The example used above is based on a ternary system, and it should be underlined that in a system with many more components, there will be an even greater number of composition fluctuations of identical energies, which will be of no interest for the nucleation of a given phase. Therefore one can expect the factor f to decrease in general, as the number of components increases.

In conclusion, it is shown that, in multicomponent alloys, it is not reasonable to expect the prefactor N_σ to be independent of the composition of the steel. The composition dependency is only qualitatively explicited here but is opposite of the more intuitive argument provided by Fujita and Bhadeshia [93], which proposes that N is expected to

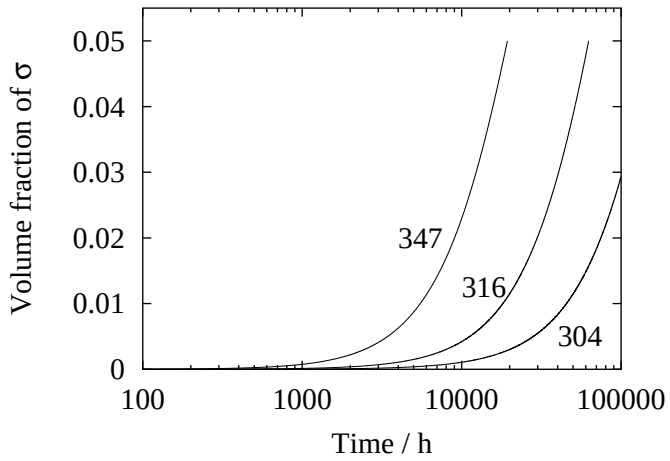

Figure 6.15: The predicted amount of σ-phase forming at 700 °C in different steels of the AISI 300 series is in better agreement with observations when allowing an increasing prefactor N as the carbon content decreases. Here, $N = 3 \times 10^{12}$ m^{-3} for 304, $N = 4 \times 10^{12}$ m^{-3} for 316 and $N = 8 \times 10^{13}$ m^{-3} for 347.

increase as the driving force (the volume fraction) for precipitation increases. In the present case, the steels with lower driving forces are actually expected to have the largest N_σ, although it should not be concluded that there is a correlation between the two.

6.6.d Other phases and difficulties

As mentioned earlier, there are significant experimental uncertainties which render difficult the task of identifying the parameters N and σ for each phase.

Of greater importance are the discrepancies between the observed behaviours of steels and the thermodynamic data on which this model relies, or the absence of such data.

Figure 6.16 shows the complete precipitation sequence for an AISI 316 steel, at 700 °C, which is in good agreement with the work of Minami *et al.* [44]. However, at 750 °C, χ phase is found experimentally, but is not predicted to form by the model. This is because, according to MT-DATA, the driving force for its formation is zero throughout the precipitation sequence.

Similar problems occur with Nb rich steels (AISI 347) in which Fe_2Nb and Fe_3Nb_3C are expected to form when Nb is in excess (chapter II). Although the formation of the former is correctly predicted, its dissolution for the latter cannot be accounted for, since there are no thermodynamic data for Fe_3Nb_3C.

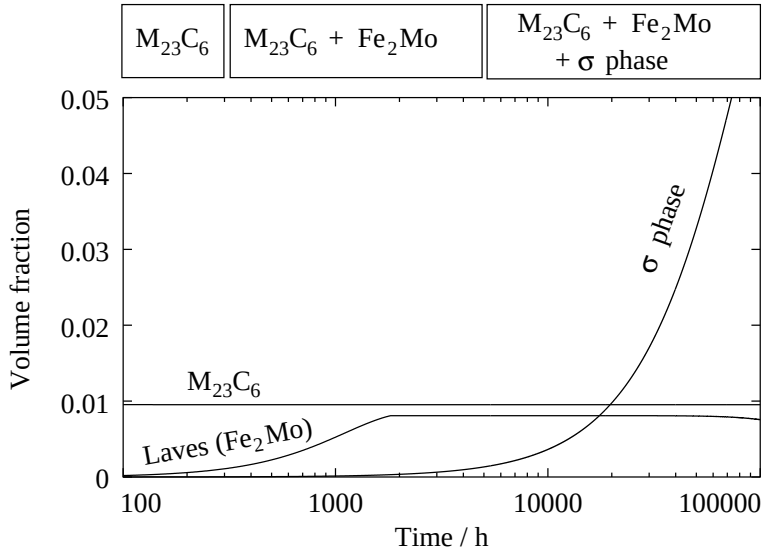

Figure 6.16: The evolution of the volume fraction of different phases in an AISI 316 steel at 700 °C, and on the upper part, the phases observed experimentally by Minami *et al.* [44].

Phases such as Cr_3Ni_2SiX or Z-phase are not represented in the SGTE database, therefore making impossible any meaningful prediction on nitrogen bearing steels.

6.7 Practical aspects of the software

Figure 6.17 illustrates the overall functioning of the software. As mentioned earlier, it is interfaced with the thermodynamic calculation package MT-DATA, and has been written so as not to implicitly incorporate knowledge about the phases. That is to say, none of the algorithms contain assumptions about what component may control the growth or dissolution of any precipitate, nor about which precipitate may form or not. Therefore any correction or addition in the databases is immediately reflected in the model, which can be used with any phase described in the thermodynamic databases.

Physical information about the phases is stored in a separate file, which contains the lattice parameter, number of atoms per unit cell, temperature dependency of the lattice parameter if known, and the nucleation parameters N and σ.

The solution treatment is modelled by assuming that equilibrium is reached at the given temperature. For example, when predicting the evolution of the microstructure of

an AISI 347 steel, it is essential to include a solution treatment, at typical temperatures of 1100-1200 °C which calculates the amount of undissolved phases and sets a new bulk composition before proceeding with the ageing.

By default, the diffusion coefficients are calculated for Fe-Cr-Ni-C alloys, as explained in chapter 4, however the user has the possibility to enter alternative values for a different system.

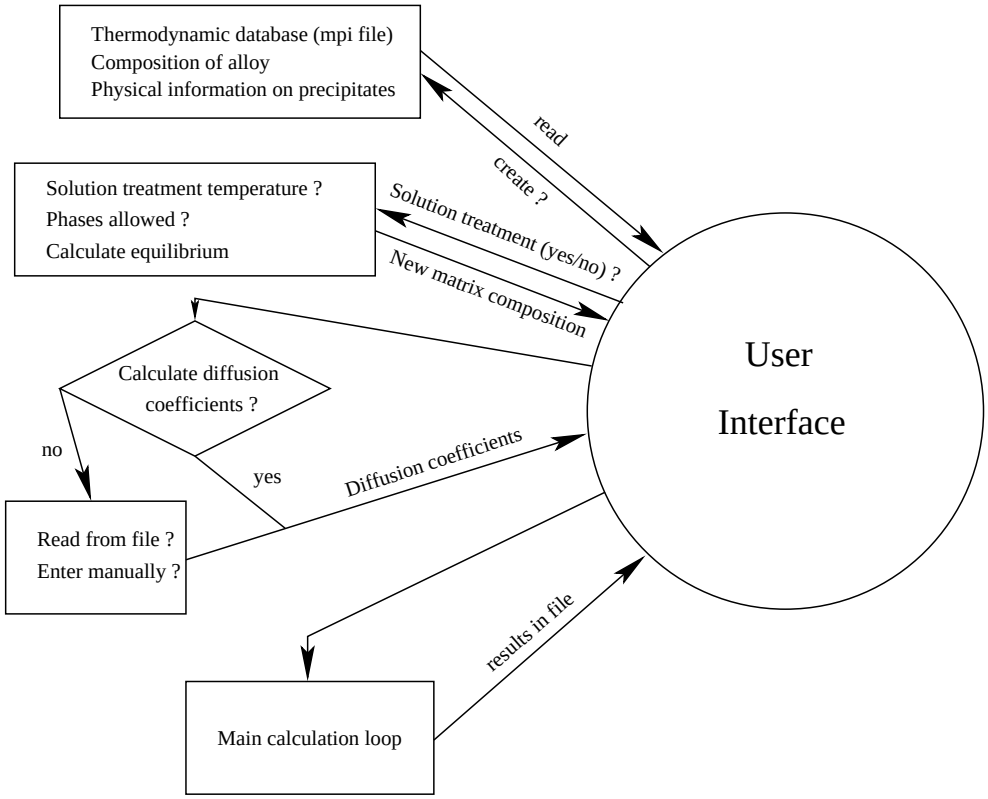

Figure 6.17: General functioning of the software developed in interface with MT-DATA, which can be used with any phase present in the SGTE databases provided that informations such as lattice parameters, interfacial energies, *etc* are present or provided.

Finally, the program is written in a modular manner which allows for easy modifications or additions.